This paper has been published in Additive Manufacturing. It can be accessed through Elsevier at https://doi.org/10.1016/j.addma.2019.03.025

Metallurgical and Mechanical Assessment of Hybrid Additively-Manufactured Maraging Tool Steels via Selective Laser Melting

H. Azizi[1], R. Ghiaasiaan[1], R. Prager[1], M.H. Ghoncheh[1], Khaled Abu Samk[1], Ante Lausic[2], Wes Byleveld[2], A.B. Phillion[1,*]

[1]Department of Materials Science and Engineering, McMaster University, 1280 Main St West, Hamilton, ON, Canada, L8S 4L7

[2]Exco Engineering, 1314 Ringwell Drive, Newmarket, ON, L3Y 9C6

*Corresponding Author: phillab@mcmaster.ca

Abstract

A complete metallurgical and mechanical assessment of additively-manufactured maraging tool steels has been undertaken, beginning with the initial powder and ending at hybrid builds. The effect of powder recycling on powder characteristics is investigated using flowability, size distribution, and density measurements. Virgin and re-used powder have similar characteristics in terms of size distribution and chemical and phase homogeneity, but no flowability. A microstructural characterization of the as-built and heat-treated samples is undertaken, showing the phase evolution, and the formation of porosity between build layers. The age-hardening response of the alloy at 490˚C and 650˚C is demonstrated to be similar to the material in the wrought condition. Finally, hybrid build scenarios are examined – maraging steel powder deposited onto C300 maraging steel, as well as H13 tool steel substrates – using digital image correlation. In both cases, the interface remains coherent without any sign of de-bonding during tensile deformation. In the case of the maraging steel powder / C300 substrate, the deformation is homogeneous throughout until failure localizes away from the interface. In the case of the maraging steel powder / H13 substrate, the deformation is predominantly within the substrate until failure localizes at the interface. A heat treatment strategy for the maraging steel powder / H13 tool steel substrate is proposed.

Keywords: Selective Laser Melting; Maraging tool steels; Hybrid AM; Metallurgy; Mechanical properties

1 Introduction

Additive manufacturing (AM) has emerged as a critical method for fabricating tooling and moulds for die casting processes. Instead of long lead times associated with delivering large blocks of forged steel, metal powder can be stocked and turned into parts of any size up to the machine's limits. Not only can AM reduce component lead time, it also improves functionality and enhances tooling customization. The greatest value add comes in the form of conformal cooling channels that match the profile of the component being cast. This gives more flexibility to mold designers in controlling heat removal and hot spots as complex cooling channels remain out of reach when using conventional tool steel machining processes.

Maraging steels (Fe-Ni base alloys) are widely used in the tool and die industry thanks to their high specific strength, high fracture toughness and good weldability. They are a material of choice for many tooling applications including plastic injection molding, high pressure die casting, punching and extrusion [1]. Heat treatment of the maraging steels involves solutionizing followed by an aging treatment. The strength of the material increases as a result of the formation of different intermetallic components upon aging. As AM is effectively a high velocity micro-welding process, it is the favorable weldability properties of maraging steel that made it a perfect candidate for AM. Subsequent heat treating after AM processing will 'wash out' the layered microstructure and tailor materials to the properties required on an application-to-application basis. Initial forays into AM with Fe-18Ni-0.03C (C300) maraging steels showed comparable strengths and properties as conventional forged bars [2-4]. Most recently, a detailed examination of microstructure and precipitation reactions in C300 during powder bed selective laser melting (PB-SLM) was conducted by Casati *et al.* [5] and Jägle et al. [6]. Casti showed that a very fine cellular-dendritic structure develops during the process, along with reverted austenite as a result of inhomogeneous distribution of alloying elements [5]. Further, Jägle showed that the post-aging mechanical properties of PB-SLM-produced material without a solutionizing treatment was comparable to material solutionized prior to aging [6]. For industrial tooling applications, however, the slow and expensive PB-SLM process is an obstacle to creating components in the >10kg range. One way to minimize cost and time is through hybrid AM [7, 8]. As the beneficial conformal cooling channels are in the upper cavity portions of tooling components, it would be preferable to machine conventionally the bulky, simple bases and then to additively manufacture on top of these bases. In this study, the effects of the selective laser melting process on the metallurgical and mechanical

properties of a commercial C300 maraging steel alloy are examined. First, the powder characteristics are summarized. Second, the metallurgical and mechanical properties of the as-built components are investigated. Finally, experimental findings concerning hybrid builds between the C300 powder and various substrates are presented. Digital Image Correlation is used to investigate the partitioning of deformation between the built layer and substrates. A post heat treatment strategy for the dissimilar joints is proposed.

2 Experimental Procedure

Materials: The C300 maraging steel powder, known as MS1, was provided by EOS in the 15-62μm particle size range. The build substrates, which were also used as one-half of the hybrid samples, were either wrought C300 maraging steel or wrought H13 tool steel. Table 1 lists the chemical composition of the materials utilized in this study.

MS1 Powder Analysis: The powder characteristics (size distribution, flowability and apparent density) were measured using a laser diffraction technique and Hall tests following ASTM standards B212 [9] and B213 [10]. Tapping was allowed for the Hall flowmeter as per standard to initiate the flow. Packs of particles were mounted, polished, carbon coated, and then imaged using scanning electron microscopy.

Additive Manufacturing: An EOS-M400 PB-SLM apparatus was used to build a series of sample coupons for metallographic examination and mechanical testing. Specifically, coupons of the MS1 powder were built on a plain carbon steel substrate with the use of support to systematically investigate the metallurgy and mechanical properties of AM-produced components. Then, the MS1 powder was built on C300 and H13 substrates without the use of support to investigate hybrid build strategies and post processing heat treatment. Process parameters were set according to the exposure parameter set 'Performance 2.0 for MS1', released by EOS. This parameter set was then optimized for the generation of high quality MS1 maraging steel parts, aiming to reduce the duration of the process while achieving excellent mechanical properties. The layer thickness was 50 μm; the powder density was 50 J/mm^3. A nitrogen, N_2, atmosphere was maintained throughout the build process.

Heat Treatment: All samples were heat treated as schematically shown in Figure 1 in a nitrogen atmosphere. For the MS1 coupons and the MS1-C300 hybrid builds, the samples were solutionized at 850 ºC for 90 min, air quenched, then aged at either 490 °C or 650 °C for different times and air

quenched. For the MS1-H13 hybrid builds, samples were first heated to 600 °C, then to 800 °C, and finally to 1030 °C, following a procedure described in [11]. For the first two stages, 10-minute thermal pauses were applied to allow the temperature to equalize throughout the sample. For the third stage, samples were held for 30 min enabling solutionizing of the MS1 build and austenitizing of the H13 substrate. The heating rate was 10 °C/min.

Metallography and Mechanical Testing: Vickers (HV) and Rockwell C (HRC) hardness testing were performed on the as-built and heat-treated samples. Samples were then cut, ground, polished in colloidal silica, and etched with a Nital 5 pct. solution. Finally, optical and electron microscopy were performed, along with electron back-scatter diffraction (EBSD) analyses. An EBSD step size of 0.1-0.2 μm was used for selected samples. Tensile testing was carried out using a 100 kN MTS servo-hydraulic machine at a strain rate of 5×10^{-4} /s with an extensometer attached to the samples. The tensile axis was parallel to the build direction. Test coupons were built as per ASTM E8 sub-size samples with 25 mm gauge length. The hybrid build coupons were machined carefully to make sure the position of the interface is at the center of the gauge length. Concurrent with the tensile tests, Digital Image Correlation (DIC) was performed; the ARAMIS 6.1 system was used to record the deformation patterns continuously in the gauge length during deformation. The Strain to fracture was measured using initial surface and final fracture surface areas, i.e. $\varepsilon_f = Ln\,(\frac{A_0}{A_f})$. The Fracture surface area was measured using SEM micrographs.

3 Results

3.1 MS1 Powder Characteristics

Metallic powder represents the initial material for the PB-SLM process and final part properties will be reflective of the powder's constituent particle characteristics (defects, chemistry, shape, and size distribution). Un-melted powder that has been fed into the build area but has not been used is collected, sieved, and recycled in subsequent builds to minimize material waste. While having not been fully melted in the process, some of the recycled particles would have experienced sufficient heat from the adjacent additively manufactured parts to distort, partially melt, or sinter to surrounding particles. This recycled powder may have different properties that potentially impact part quality in subsequent builds.

Figure 2 presents the SEM micrographs of the MS1 maraging steel powder in the (a) virgin and (b) re-used conditions having been recycled approximately 30 times with virgin powder used to

top up 3 times in this period accounting for 15% of the total end mass of used powder. There is a notable difference in the morphology between the two states. The virgin powder particles are uniformly distributed with a globular morphology whereas the re-used powder particles are partially elongated in shape and/or melted/agglomerated with other particles. In both cases, a few of the particles contained defects, mainly trapped gas that is likely from the atomization process, shown by white arrow in Figure 2c. It should be noted that these defects appear rare; only very few defected particles were found amongst more than 1000 imaged particles in both the virgin and re-used states. The particle characteristics presented in Table 2 show that both particles are quite similar in size distribution and apparent density. However, the re-used powder had no flowability as compared to the virgin one thanks to loss of roundness and small particle sintering as seen in Figure 2b. Although this finding would advise against reusing powders, experience has shown that the powder distribution mechanism of the EOS M400 and similar systems is able to adequately spread the powder during recoating of the build volume by modifying factors such as dosing and recoating speed. These are common practice with negligible influence on porosity level.

To provide a detailed investigation of the powder, the rounded virgin particle shown in Figure 3a was chosen for further analysis. In tilted SEM view, Figure 3b, the particle is seen to contain significant substructure. This substructure is magnified in Figures 3c,d to highlight the grain boundaries and phase maps of a selected area within the particle. As can be seen, high angle grain boundaries (>15º misorientation) given by black lines demonstrate the very fine grain structure within the powder particle. Further, there is approx. 10% retained austenite located at the grain boundaries and coloured in red. An XRD analysis of the powder confirmed the presence of austenite in the MS1 powder, and further indicated no significant change in the austenite volume fraction between the virgin and re-used states. The given Inverse Pole Figure (IPF) map, Figure 3e, shows the presence of grain boundaries within the particle. Thus, even though the particles are small, they obviously contained numerous solidification nucleation events. Finally, a low degree of partitioning of alloying elements is evident within the particle. As shown in Figure 3f (EDS area scan for Ti), there is no major area of segregation. Further, all of the partitioning occurs concurrent to the location of the retained austenite constituents (red phase in Figure 3d).

3.2 Microstructural Analysis of As-Built Components

MS1 coupons built on a plain carbon steel substrate: Figure 4a shows a three-dimensional optical view of one of the MS1 coupons in the as-built state. The etched micrograph shows limited

porosity (less than 1.0 vol.%) throughout, along with some details of the structure. A closer examination, Figure 4b (parallel to the build direction) and Figure 4c (normal to the build direction) clearly reveals the sequential powder layers as well as the hatch pattern used by the laser to melt the powder. Further, the porosity is relatively small, <75 μm, and is mainly located at the boundary between the layers. The IPF map, Figure 4d, reveals the lath martensite structure. The retained austenite volume fraction in the as-built state, Figure 4e, was found to be approx. 10 vol.%. The presence of this retained austenite was confirmed through XRD analysis.

Hybrid MS1-C300 and MS1-H13 builds: Figure 5 shows optical micrographs of the as-built hybrid samples of MS1-C300 and MS1-H13. Beginning with the macro-scale, Figure 5a,c, the additively manufactured material is clearly visible from the presence of porosity. The interfaces are shown by the horizontal black lines. While the boundary between MS1-H13 qualitatively looks more porous than the MS1-C300 build, the porosity remained less than 1.0 vol.% in both builds. Away from the interface, the porosity was evenly distributed across the entire additively manufactured region, matching the observations found in the MS1 coupons presented above. The high resolution micrographs of etched samples, Figures 5b,d, reveal very coherent and diffuse boundaries where the alloys have joined. Detailed images of the diffuse MS1/H13 interface are shown in Figure 10 and discussed later on. Further evidence of a strong dissimilar bond is given by a lack of porosity at the coupon sample part/substrate interface.

3.3 Age Hardening Behaviour

MS1 coupons built on a plain carbon steel substrate: Figure 6 presents Vickers (HV) and Rockwell C (HRC) hardness curves for two MS1 coupons as well as two conventionally wrought processed maraging steel C300 samples. The hardness measurements were carried out after age hardening at two different temperatures: 490 °C and 650 °C. Prior to the aging heat treatments, all samples were solution annealed at 850 °C for 90 min followed by an air quench. From this figure, a number of salient observations can be made. First, the MS1 coupons and wrought C300 samples age harden in a very similar fashion, with the two curves at each temperature nearly overlapping. Second, although the hardness initially increases with aging time at either temperature, aging at 650°C leads to reaching a peak hardness sooner than aging at 490°C. The peak hardness of approximately 450 HV (~44 HRC) is reached in less than 10 minutes at 650 °C, after which the hardness begins to decrease. At 490˚C, the hardness continues to increase even after 4000 minutes (~ 67 hours) of aging; it is unclear if the peak hardness is reached at this time. This slow aging process can be

attributed to the effect of temperature on the diffusion of alloying elements (Ni, Ti and Al) in the iron matrix and to/from the Ni rich precipitates (Fe (Mo,Ni,Al)$_3$) and Ni$_3$ (Ti,Mo) that lead to increased strength [6, 13]. Third, at 490˚C, there appears to be a plateau in the hardening behaviour between 1 and 10 min. This plateau could be used to achieve desirable hardness level after heat treatment of an additively manufactured component even in regions with varying wall thickness and thus different heating rates.

Hybrid MS1-C300 and MS1-H13 builds: The hardness of the hybrid MS1-C300 builds is expected to match the results shown for the MS1 coupons, Figure 6. The interesting age hardening behaviour is seen in the MS1-H13 hybrid. Given the difference in composition between MS1 and H13, the built layer and substrate are expected to show significant difference in hardness. The evolution in hardness with processing for the MS1 build layer and the H13 tool steel substrate are shown in Figure 7. In the as-built state, the values were found to be 430.0 ± 12.0 HV for the MS1 build and 225.0± 5.0 HV for the H13 substrate. After the solutionizing/austenitizing treatments, stage I in Figure 1b, these hardness values changed to 286.0 ± 15.0 for the MS1 build and 608.0 ± 14.0 HV for the H13 substrate. At this point, the MS1 maraging steel is now soft and ductile, in a solutionized state without precipitates while the H13 tool steel is very hard and brittle, having as-quenched martensite structure. The aging/tempering stages, stage II in Figure 1b, thus results in age-hardening of the MS1 but tempering of the H13 substrate. As can be seen in Figure 7, heat treatment of the hybrid at 650˚C results in an increase in hardness for the MS1 build but a loss in hardness for the H13 substrate. For such a hybrid build, the key is to identify a middle ground where the MS1 has sufficiently age hardened and the H13 has sufficiently tempered so that they contain equivalent properties. This is necessary to avoid fracture in the substrate material. Referring again to Figure 7, after ~60 min. of aging time, the hardness values are nearly equivalent in both steels, at ~ 410 HV. Thus, a heat treatment schedule of 60 min at 650 °C is proposed for MS1-H13 hybrids, and was chosen for further characterization and tensile testing.

3.4 Microstructure Analysis of the Hybrid Builds in the Heat-Treated State

MS1-C300 hybrid builds

Figure 8 shows the microstructure of the MS1-C300 hybrid build after the 60 min heat treatment at 650 ˚C. The images were acquired via SEM/EBSD. The build direction is vertical, and the boundary between the built MS1 and C300 substrate is denoted by two grey arrows on either extremes of (a) and (d). As can be seen in Figure 8a (grain boundary map), the material contains

fine grains, and the boundary between the substrate and build is diffuse. The substrate has a relatively finer structure as compared to the built microstructure. The grains in both substrate and the build are qualitatively randomly oriented, Figure 8b (IPF map of ferrite). An interesting observation is the presence of approximately 25% retained/reverted austenite throughout the sample, and heavily concentrated at the C300/MS1 interface. The austenite distribution is given in Figure 8c (IPF map of austenite), with additional details regarding the concentrated austenite at the interface visible in Figure 8d. Figure 15 shows high-resolution SEM images of the MS1 and C300 microstructure on either side of the interface identified by dark indents at the center. Although the EBSD image shown in Figure 8b indicated a small difference in structure between the built and substrate layers, it can be seen through these images that the underlying constituents show identical lath microstructure. Finally, there is very little porosity present, reinforcing the observations made in Figure 5 that the interface is a sound metallurgical bond.

MS1-H13 hybrid builds

Figure 9 shows the SEM/EBSD micrographs of the MS1-H13 hybrid build heat treated at 650 ºC for 60 min; the interface is identified by white indents at the center. As can be seen, the microstructure is very fine in both the MS1 built layer as well as the H13 substrate, with very low porosity at the interface. Although the built layer and substrate are different materials, the microstructure throughout is martensite in nature giving a similar appearance. Further, the crystallographic orientation is qualitatively similar throughout the hybrid build, Figure 9b. To further analyze the MS1-H13 hybrid microstructure, high-resolution SEM analysis of a region near the interface (white box in Figure 9a) was carried out. Figure 10a shows clearly the diffuse nature of the interface, along with defects – a pore with un-melted particles trapped in them (white arrow) and trapped gas with rounded shape (red arrow). Figures 10b,c, and d show evolution of the microstructure across the interface, and the clear transition from a heat treated wrought H13 base plate to an as-printed and heat treated MS1 build. In the substrate, Figure 10b, the microstructure consists of tempered martensite with carbides highlighting presumably prior austenite grain boundaries as well as lath boundaries. This microstructure is in contact with lath structure of a mixture of the MS1 and H13 alloys at the interface, Figure 10c, and a more defined lath structure further into the interface towards the MS1 side, Figure 10d.

Solute Variation across the Interface: A chemical analysis of the interface area was performed to shed further light on the depth of the transition region. Figure 11 shows an EDS line scan across

the interface of both hybrid builds, MS1-C300 in a, and MS1-H13 in b. The centre of the plot denotes the centre of the interface (dashed lines). It is evident from Figure 11a that there is no gradient in chemistry in the similar MS1-C300 hybrid as all the major alloying elements (Ni, Co and Mo) are within the designated range of composition given in Table 1. The situation is much different for the MS1-H13 hybrid, Figure 11b. Here, there is a transition region of ~200 μm where the chemical composition changes abruptly from the MS1 containing Ni, Mo, and Co to the H13 containing Cr. The abrupt change in composition is accompanied with significant change in microstructure, as shown in Figure 10, which can have a significant impact on mechanical properties in the heat-treated state. Note that the transition is not instantaneous due to diffusion between the built layer and the substrate. As Cr diffuses faster than Ni/Mo in Fe, it is seen to have travelled further into the MS1 side of the hybrid than the other elements.

3.5 Mechanical Testing of Heat Treated Hybrids

Figure 12 shows engineering stress / engineering strain curves acquired from tensile tests of the MS1-C300 and MS1-H13 hybrid builds, heat treated at 650˚C for 60 min., along with specimens machined directly from the C300 maraging steel and heat treated at both 490˚C for 360 min. and 650˚C for 60 min. Two tests were performed for each material except the MS1-C300 hybrid. It should be noted that tensile test samples for the mechanical analysis were machined such that the gauge length was divided equally between the substrate and the build.

Being in wrought form, the C300 maraging steel specimens are expected to show the best properties. As can be seen, heat treatment at 490˚C provided the C300 material with an ultimate tensile strength (UTS) of 2.1 GPa. At 650˚C, the UTS had decreased to 1.2 GPa. The loss in UTS at the higher temperature is accompanied by an increase in uniform elongation from 2 to 10 % as the aging temperature was increased. Examining the additively-manufactured hybrid builds, it can be seen that for all cases, the UTS remained within 10% of that for the wrought alloy. Achieving a similar UTS in PB-SLM produced hybrid steels as compared to wrought form is a major accomplishment. In terms of the ductility, it can be seen that the MS1-C300 hybrid, the MS1-H13 hybrid, and the C300 wrought material all have similar ductility within experimental reproducibility. Some observed differences are likely a result of porosity and/or grain texture differences within the built parts.

It is desirable to not only characterize the overall stress/strain behaviour of the hybrid builds, but also to observe the localization of strain through digital image correlation in a hybrid build. Figures

13 and 14 show strain maps of the MS1-C300 and MS1-H13 samples at (a) the UTS and (b) just before fracture. The corresponding optical micrograph for each sample is given in (c), while (d) plots the average transverse strain along the gauge length. Beginning with the MS1-C300 sample, it can be seen that there is uniform deformation in both the substrate and the build layer at the point when the UTS is reached, Figure 13a, however, there is greater strain in the MS1 build layer owing to the fact that it has a ~10% lower flow stress as shown in Figure 12a and more porosity in the initial state. Beyond the UTS, strain localizes in one part of the build layer, Figure 13b, leading to fracture. The corresponding optical micrograph, Figure 13d, shows the distribution of porosity throughout the build layer but none in the substrate. The pre-existing pores in the built part grew as a result of the tensile deformation. The variation in strain along the length of the gauge region (averaged across the width) at the point of yielding, at the UTS, and just before fracture are shown in Figure 14c. As can be seen, there is clear localization at the point of fracture. Further, even the uniform strain in the MS1 built layer is considerably greater than the strain in the C300 substrate. Turning now to the MS1-H13 hybrid, considerable differences can be seen as compared to the MS1-C300 hybrid. First, at the UTS, Figure 14a, there is greater strain in the substrate as compared to the build layer. By the time fracture is reached, Figure 14b, the strain has localized to the dissimilar joint. Second, like Figure 13d, there is considerable porosity in the build layer of the MS1-H13 hybrid, Figure 14d, just prior to fracture. However, the failure takes place directly across the substrate-build layer interface. The average strain distribution, Figure 14c, also shows clearly the localization of the strain to the interface. Strain to fracture was also measured for both cases, indeed, confirming a much lower strain to fracture, 0.27 ± 0.02, for the MS1-H13 build as compared with the MS1-C300 build with 0.50 ± 0.01 strain to fracture.

4 Discussion:

In the past few years, a few studies [3, 4, 14, 15, 16] have been carried out to determine the effects of processing parameters and heat treatment on the mechanical properties of this system and thus to establish a process window for PB-SLM of this alloy. Development of the processing window has mostly relied on the bulk density and hardness data. To give an example, Mutua et al. [14] proposed a power density of 60-160 J/mm^3 for PB-SLM of MS1. The results shown in this study indicate that lower power densities also produce sound material with similar microstructural features (elongated grains, limited porosities, and retained austenite)

Solutionizing and aging treatments however make several changes to the microstructure of the maraging steel including formation of very fine precipitates and austenite reversion. The former contributes to higher hardness while the latter improves ductility at the expense of strength. In this study, the precipitation reaction were captured indirectly via the increase in hardness observed during heat treatment, Figure 6. Further, an increase in austenite content was observed using the EBSD analyses, Figure 8. Although the trend in hardness is in agreement with other published data [3, 5, 17], the results on the austenite fraction seem to indicate the importance of the formation of this phase in achieving good ductility in the PB-SLM components.

Now turning into the hybrid builds, a significant difference in fracture behavior between the MS1-C300 and MS1-H13 builds was observed. In the former, fracture happened in the built part while in the latter, the interface was the weakest point. This difference in behaviour is due to the combination of differences in microstructure and in chemical composition across the interface. In the MS1-C300 hybrid, the constituent lath microstructure is identical on the built and substrate sides, Figure 15, and there is very little gradient in alloy composition across the interface, Figure 12a. In contrast, there is a sharp transition in both microstructure and chemical composition across the MS1-H13 interface, as shown in Figures 10 and 12. Finally, there may also be increased porosity at the MS1-H13 interface due to the dissimilar join, as seen in Figure 5c. Thus, in summary, the fracture behavior of the MS1-H13 hybrid build is influenced by a combination of interfacial features resulting localizing of strain and fracture in this region. In contrast, fracture in the MS1-C300 hybrid is controlled by void growth and coalescence in the built layer.

A similar failure at the MS1-H13 hybrid interface was previously reported by Cyr et al. [18]. In their study, the aging treatment was performed at 490 °C for 6 hrs as recommended by the metal powder vendor [19]. Combined, the study by Cyr and this work demonstrate that MS1-H13 hybrids can be heat treated at a range of temperatures to give the desired combination of strength and ductility. However, care must be taken in choosing the heat treatment time to ensure that the hardness across the interface remains similar.

5 Conclusions

In this study, a metallurgical and mechanical assessment of the powder bed selective laser melting of MS1 maraging steels, and hybrids has been undertaken. The major findings of this study are as follows:

1. Virgin and re-used powders have similar characteristics in terms of size distribution and chemical homogeneity. However, the re-used powder has no flowability.
2. The age-hardening response of the PB-SLM MS1 at 490˚C and 650˚C is demonstrated to be similar to the material in the wrought condition.
3. Hybrid MS1-C300 and MS1-H13 builds can also be built and heat treated to show similar properties as the wrought MS1 material.
4. Hybrid MS1-H13 builds fracture at the interface because of a combination of chemical and microstructural inhomogentity in this region, along with increased porosity; hybrid MS1-C300 builds fracture in the built layer due to porosity between the built layers.

The results of this study demonstrate the possibility of using hybrid MS1-H13 components for tool steel applications, utilizing additively manufactured MS1 for conformal cooling built on top of inexpensive H13 as die structure support. However, the heat treatment must be carefully designed to achieve desired properties.

6 Acknowledgements

The authors acknowledge funding provided by the Natural Sciences and Engineering Council of Canada and Exco Engineering Ltd. in support of this research.

7 References

[1] ASM Handbook, Volume 4, Heat treatment, 1991, in: Heat Treating of Maraging Steels by Michael Schmidt and Kurt Rohrbach, Carpenter Technology Corporation.

[2] M. Stanford, K. Kibble, M. Lindop, D. Mynors, C. Durnall, An investigation into fully melting a maraging steel using direct metal laser deposition (DMLS), Steel Research International. (2008) 847–852.

[3] K. Kempen, E. Yasa, L. Thijs, J.-P. Kruth, J. Van Humbeeck, Microstructure and mechanical properties of Selective Laser Melted 18Ni-300 steel, Physics Procedia. 12 (2011) 255–263. doi:10.1016/j.phpro.2011.03.033.

[4] G. Casalino, S.L. Campanelli, N. Contuzzi, A.D. Ludovico, Experimental investigation and statistical optimisation of the selective laser melting process of a maraging steel, Optics & Laser Technology. 65 (2015) 151–158. doi:10.1016/j.optlastec.2014.07.021.

[5] R. Casati, J.N. Lemke, A. Tuissi, M. Vedani, Aging Behaviour and Mechanical Performance of 18-Ni 300 Steel Processed by Selective Laser Melting, Metals. 6 (2016) 218. doi:10.3390/met6090218.

[6] E.A. Jägle, P.-P. Choi, J.V. Humbeeck, D. Raabe, Precipitation and austenite reversion behavior of a maraging steel produced by selective laser melting, Journal of Materials Research. 29 (2014) 2072–2079.

[7] L. Yan, W. Cui, J.W. Newkirk, F. Liou, E.E. Thomas, A.H. Baker, J.B. Castle, Build Strategy Investigation of Ti-6Al-4V Produced Via a Hybrid Manufacturing Process, JOM. 70 (2018) 1706–1713. doi:10.1007/s11837-018-3009-7.

[8] J. Hur, K. Lee, Zhu-hu, J. Kim, Hybrid rapid prototyping system using machining and deposition, Computer-Aided Design. 34 (2002) 741–754. doi:10.1016/S0010-4485(01)00203-2.

[9] ASTM B213 - 17 Standard Test Methods for Flow Rate of Metal Powders Using the Hall Flowmeter Funnel.

[10] ASTM B213 - 17 Standard Test Method for Apparent Density of Free-Flowing Metal Powders Using the Hall Flowmeter Funnel.

[11] Böhler-Uddeholm H13 tool steel data sheet.

[12] G. Jacob, C. Brown, A. Donmez, S. Watson, J. Slotwinski, Effect of powder recycling on stainless steel powder and built material properties in metal powder bed fusion processes, NIST Advanced Manufacturing Series 100-6, Feb. 2017. doi: 10.6028/NIST.AMS.100-6.

[13] E.A. Jägle, Z. Sheng, L. Wu, L. Lu, J. Risse, A. Weisheit, D. Raabe, Precipitation Reactions in Age-Hardenable Alloys During Laser Additive Manufacturing, JOM; New York. 68 (2016) 943–949. doi:http://dx.doi.org.ezproxy.library.ubc.ca/10.1007/s11837-015-1764-2.

[14] J. Mutua, S. Nakata, T. Onda, Z.-C. Chen, Optimization of selective laser melting parameters and influence of post heat treatment on microstructure and mechanical properties of maraging steel, Materials & Design. 139 (2018) 486–497. doi:10.1016/j.matdes.2017.11.042.

[15] Y. Bai, Y. Yang, D. Wang, M. Zhang, Influence mechanism of parameters process and mechanical properties evolution mechanism of maraging steel 300 by selective laser melting, Materials Science and Engineering: A. 703 (2017) 116–123. doi:10.1016/j.msea.2017.06.033.

[16] J. Suryawanshi, K.G. Prashanth, U. Ramamurty, Tensile, fracture, and fatigue crack growth properties of a 3D printed maraging steel through selective laser melting, Journal of Alloys and Compounds. 725 (2017) 355–364. doi:10.1016/j.jallcom.2017.07.177.

[17] J.M. Pardal, S.S.M. Tavares, M.P. Cindra Fonseca, M.R. da Silva, J.M. Neto, H.F.G. Abreu, Influence of temperature and aging time on hardness and magnetic properties of the maraging steel grade 300, J Mater Sci. 42 (2007) 2276–2281. doi:10.1007/s10853-006-1317-8.

[18] E. Cyr, H. Asgari, S. Shamsdini, M. Purdy, K. Hosseinkhani, M. Mohammadi, Fracture behaviour of additively manufactured MS1-H13 hybrid hard steels, Materials Letters. 212 (2018) 174–177. doi:10.1016/j.matlet.2017.10.097.

[19] EOS MaragingSteel MS1, Material data sheet, EOS GmbH - Electro Optical Systems, 2017.

8 Tables

Table 1: Chemical composition of the materials used for this study

Alloy	Fe	Cr	Ni	Mo	Co	Al	Mn	Si	V	C
C300 / MS1	Bal.	0.5	17-19	4.5-5.2	8.5-9.5	0.05-0.15	0.1	0.1	-	0.03
H13	Bal.	5.3	-	1.3	-	-	0.4	1.0	0.9	0.39

Table 2: Apparent density (AD), flowability and size characteristics of virgin and re-used MS1 powder measured using the Hall test and laser diffraction

Powder	AD, (g/cm^3)	Flow-ability[1] (sec)	d_{10}, µm	d_{50}, µm	d_{90}, µm
MS1 Virgin	4.20	15.84	18	35	54
MS1 Re-used	4.24	None	15	33	51

[1] Flowability of typical powders used for powder metallurgy products is about 30 sec.

9 Figures

Figure 1: Schematic of the heat treatment procedure of (a) MS1-C300 and (b) MS1-H13 hybrid builds. AirQ: Air quench.

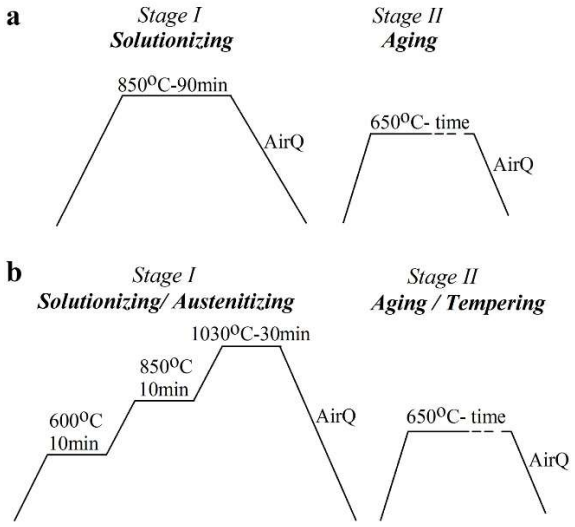

Figure 2: Secondary electron SEM images of the (a) virgin and (b) re-used MS1 maraging steel powder used in this study, and (c) porosity within the polished particle in the virgin powder.

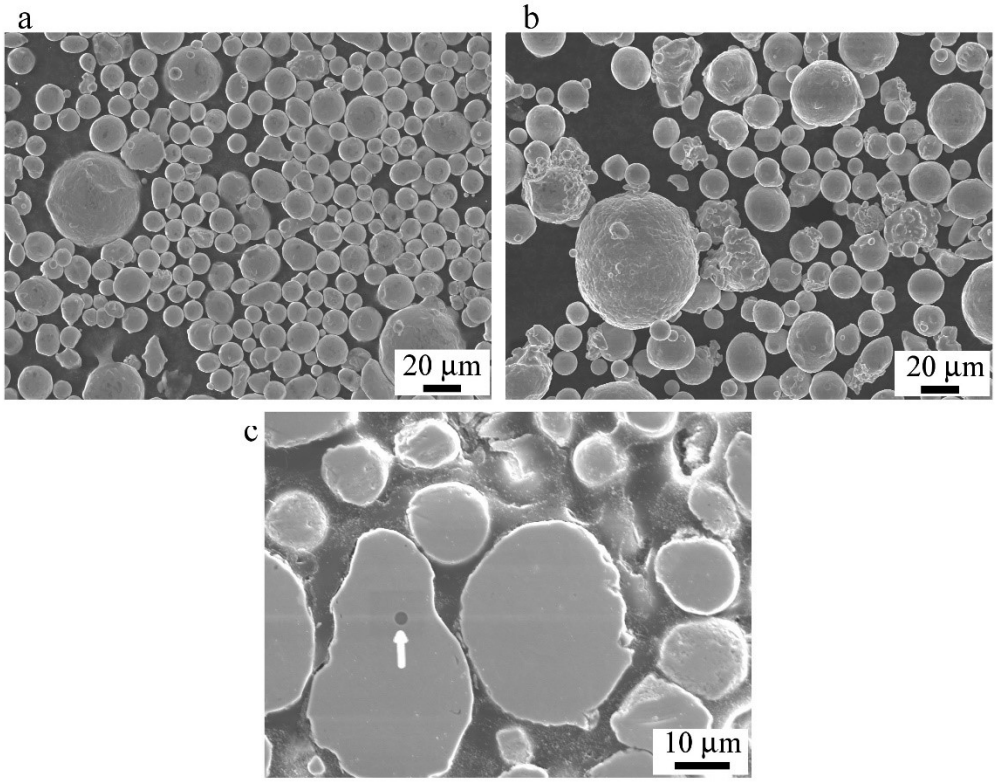

Figure 3: Cross-section of an MS1 particle, (a) SEM image with (b) surface topography and (c) reconstructed SEM from tilted particle and (d) band contrast map with grain boundaries (2-15º: white, > 15° black lines) with corresponding (e) inverse pole figure map and (f) EDS map of Ti. Note that the red colour in (d) identified the austenite phase that has partitioned to the grain boundaries.

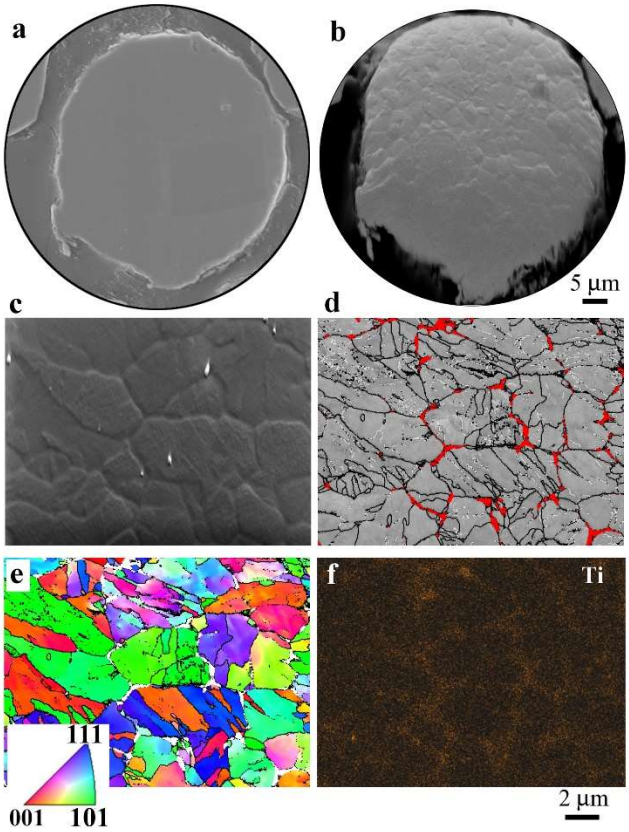

Figure 4: Microscopy of the SLM-built MS1 coupons: (a) composite optical 3D image; (b,c) optical micrographs parallel and normal to the build direction; (d) typical IPF map of the as-built sample with (e) corresponding austenite phase map of the as-built sample. The layer thickness is 50 μm. Porosity in (b) and (c) is mostly located between the layers. The arrows indicate the build direction.

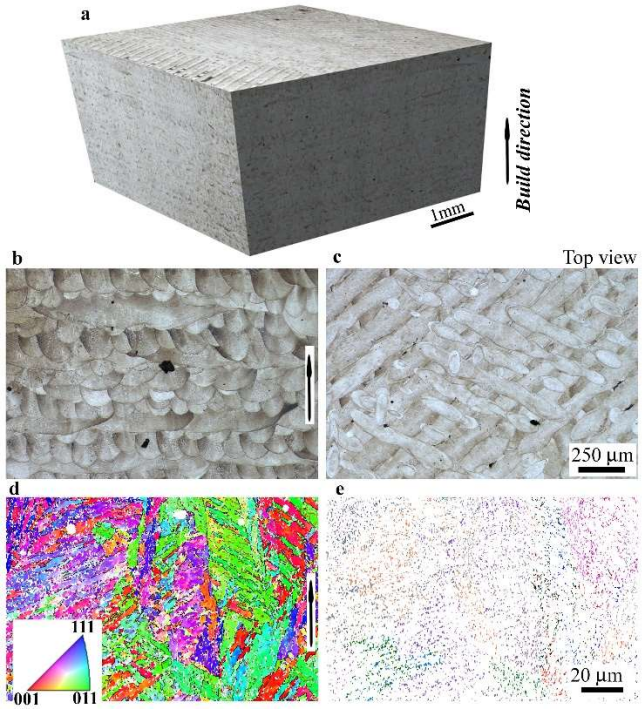

Figure 5: Micrographs of the hybrids of (a,b) MS1-C300 maraging steels, and (c,d) MS1 maraging steel-H13 tool steel in the as-built condition. The interfaces are shown as dashed lines in (a,c).

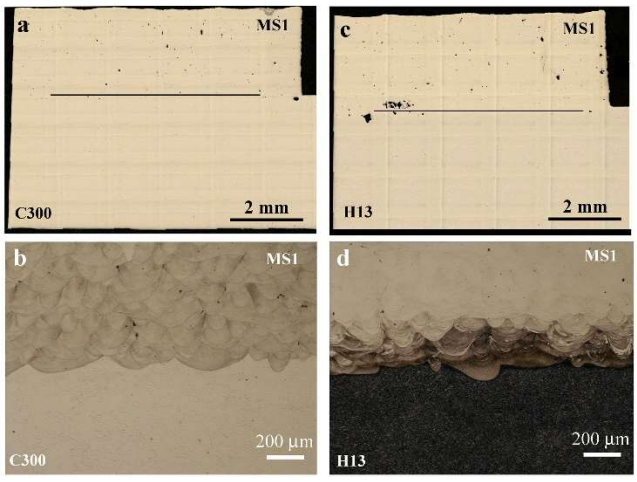

Figure 6: (a) Vickers (HV) and Rockwell C (HRC) hardness curves for both the as-built SLM and conventional wrought C300 samples after artificially aging at 490°C and 650°C. Note that all samples were solution annealed at 850 ºC for 90 min prior to age hardening (some of the error bars are within the symbols).

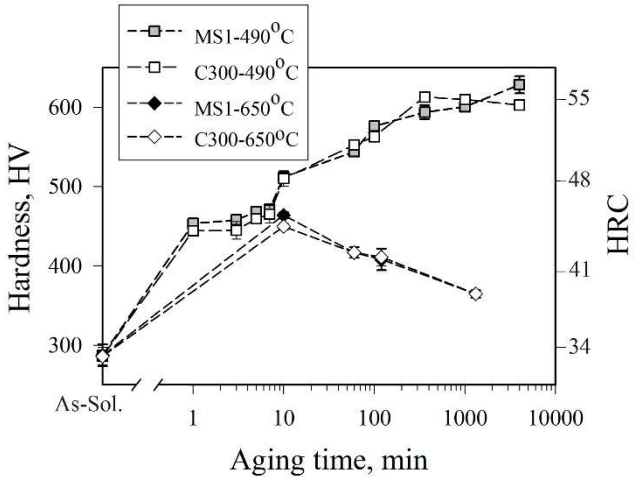

Figure 7: Variation in Vickers hardness with time for the MS1 built layer and H13 substrate after ageing at 650°C (some of the error bars are within the symbols).

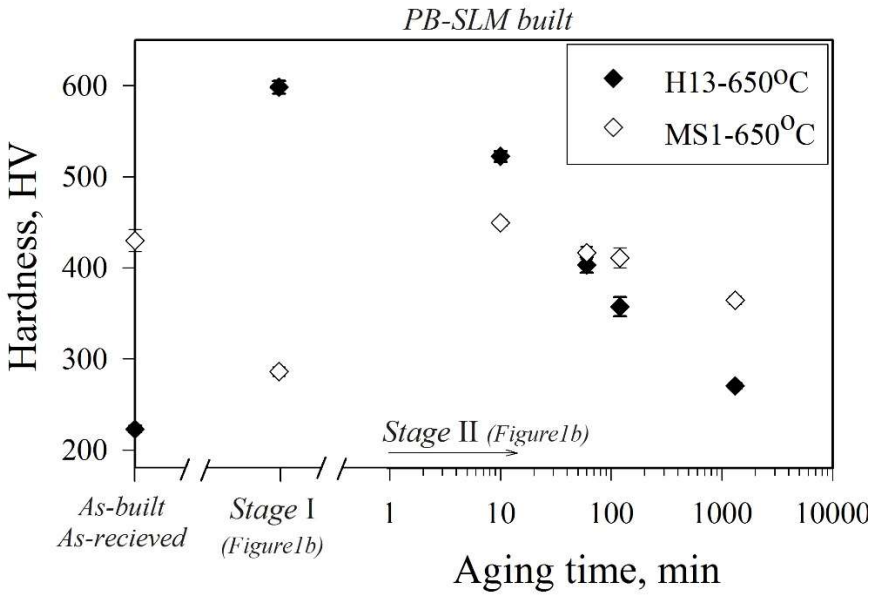

Figure 8: Microstructure of the MS1-C300 hybrid build, heat treated for 60 min at 650˚C: (a) EBSD grain boundary map, corresponding IPF maps of (b) ferrite and (c) austenite phases. (d) Phase map (ferrite: blue, austenite: red). The austenite fraction is ~25 %.

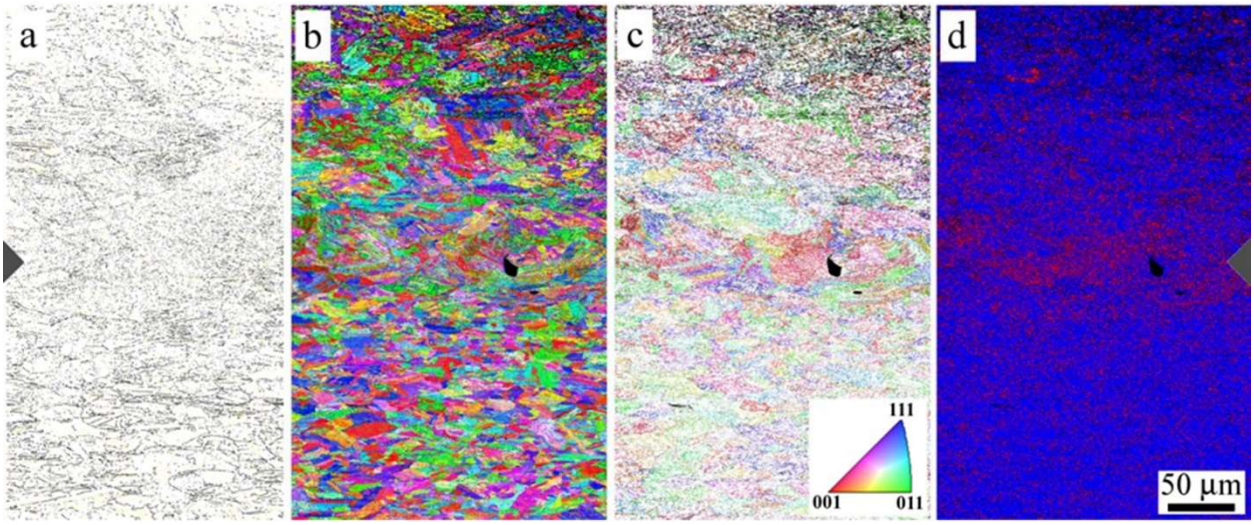

Figure 9: (a) SEM micrograph of the MS1-H13 hybrid build, heat treated for 60 min at 650˚C, and (b) corresponding EBSD grain boundary map.

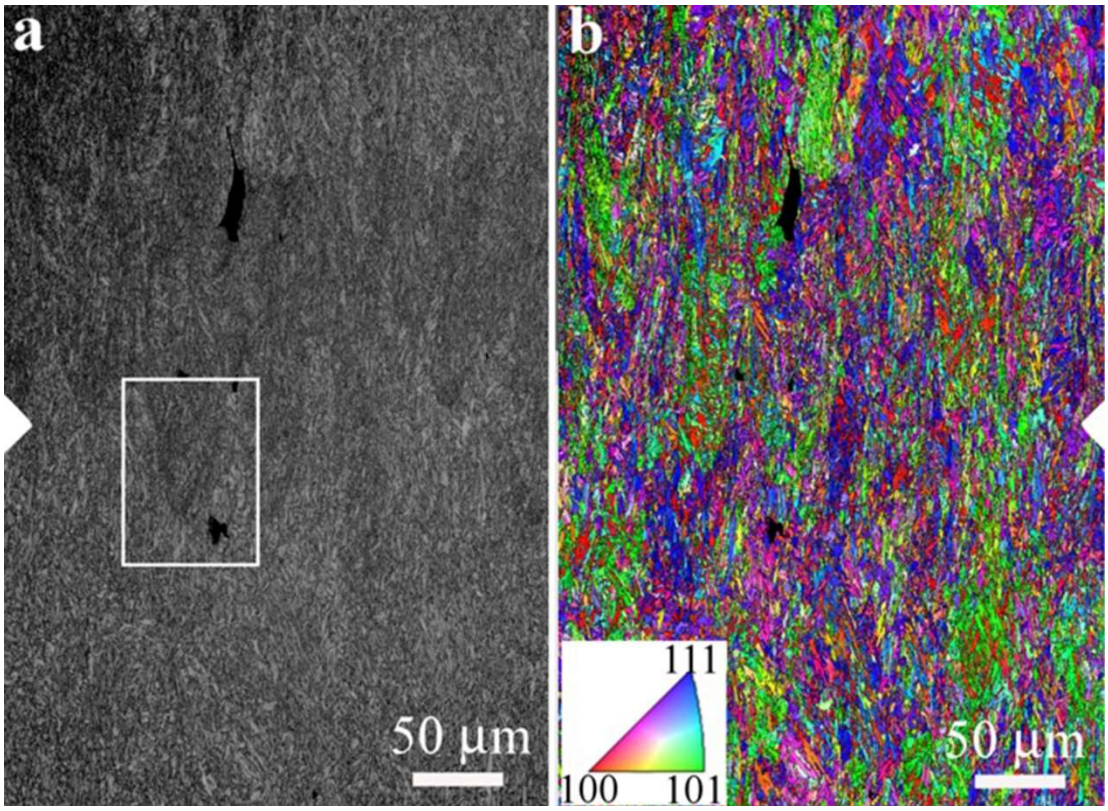

Figure 10: (a) SEM micrograph of the interface area between MS1 and H13. A pore near an un-melted particle is shown by a white arrow, while rounded trapped gas is shown by red arrow. Different areas of interest are highlighted in (a) as (b) H13 matrix, (c, d) interface area where the two alloys mix.

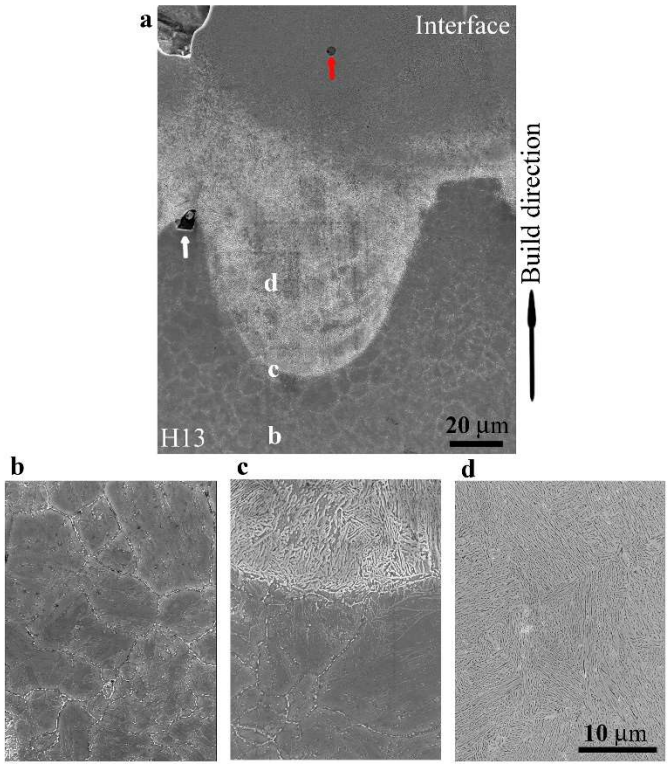

Figure 11: EDS analyses of the interface area between different hybrid builds, (a) MS1-C300 and (b) MS1-H13.

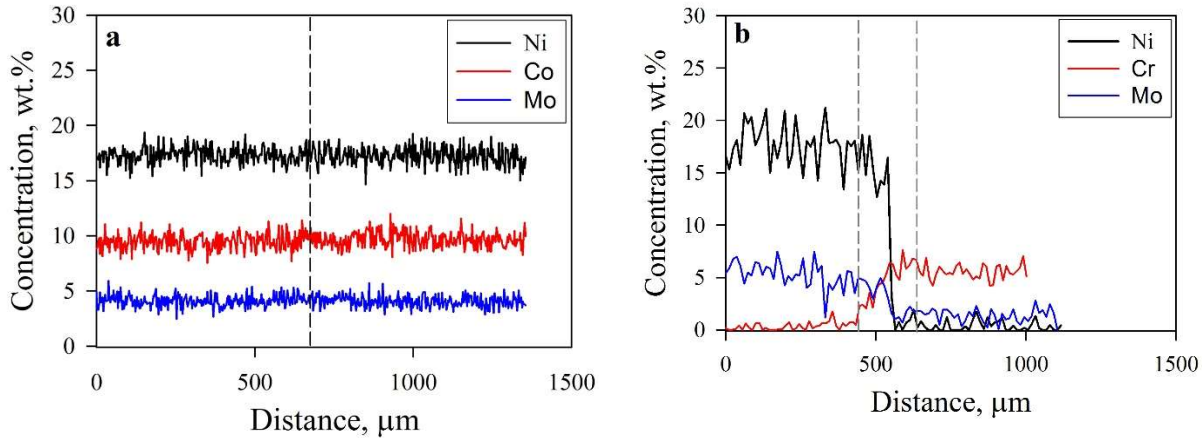

Figure 12: Engineering stress/strain curves acquired from tensile tests of MS1-C300 and MS1-H13 hybrid builds. The results of C300 are also given for comparison purposes.

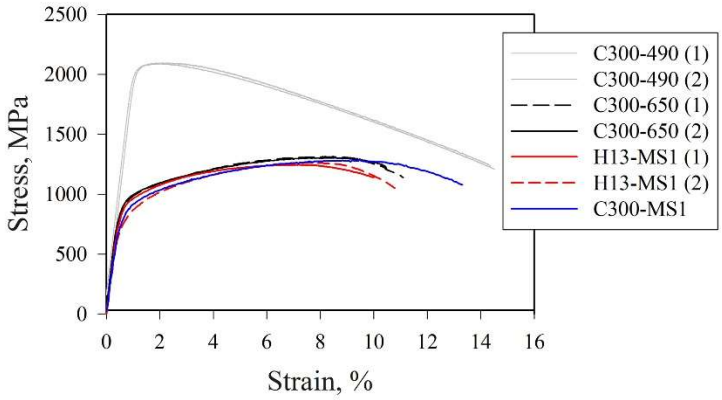

Figure 13: DIC strain map of MS1-C300 hybrid build during tensile deformation at (a) UTS and (b) just before fracture. (c) The corresponding optical micrograph after fracture. (d) Strain distribution map along the gauge length of the hybrid tensile sample. The inert image in (d) shows the sample with speckle pattern just before fracture. The vertical dashed line denotes the interface position.

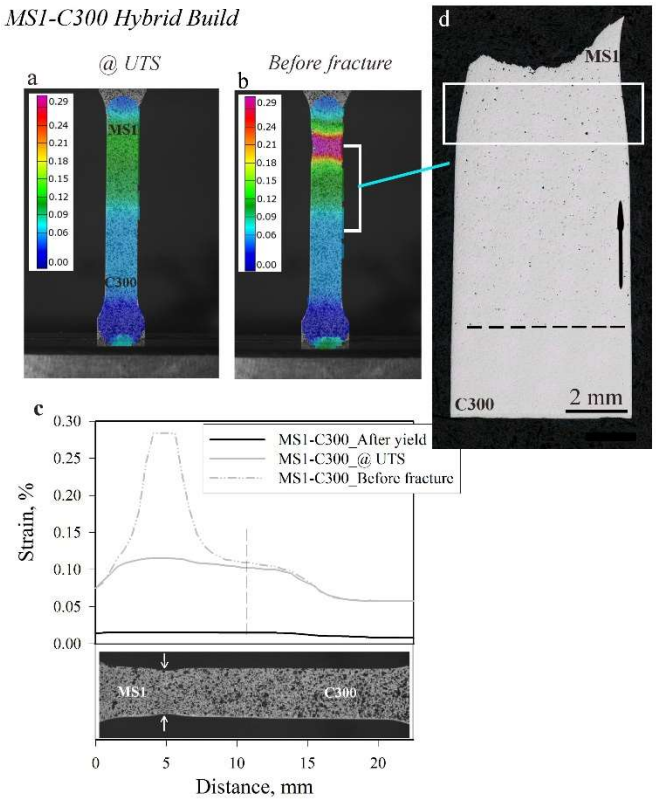

Figure 14: DIC strain map of MS1-H13 hybrid build during tensile deformation at (a) UTS and (b) just before fracture. (c) The corresponding optical micrograph after fracture. (d) Strain distribution map along the gauge length of the hybrid tensile sample. The inert image in (d) shows the sample with speckle pattern just before fracture. The vertical dashed line denotes the interface position.

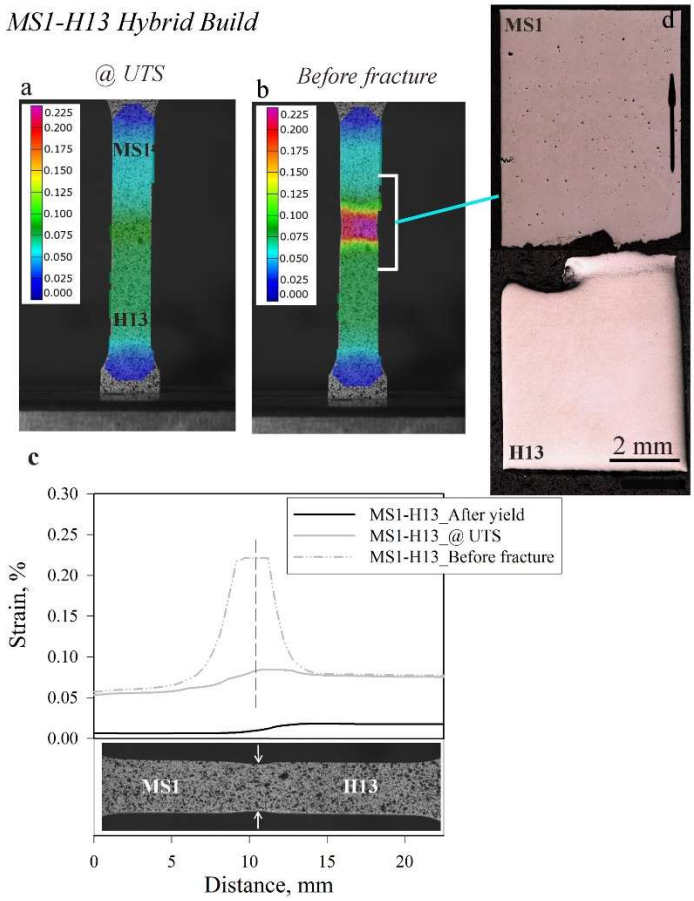

Figure 15: Microstructure of maraging steel in (a) C300 substrate and (b) MS1 build.